



UNIVERSITY OF LEEDS

This is a repository copy of *On the relative importance of shocks and self-gravity in modifying tidal disruption event debris streams*.

White Rose Research Online URL for this paper:

<https://eprints.whiterose.ac.uk/204818/>

Version: Published Version

---

**Article:**

Fancher, J. [orcid.org/0009-0008-5847-9778](https://orcid.org/0009-0008-5847-9778), Coughlin, E.R. [orcid.org/0000-0003-3765-6401](https://orcid.org/0000-0003-3765-6401) and Nixon, C.J. [orcid.org/0000-0002-2137-4146](https://orcid.org/0000-0002-2137-4146) (2023) On the relative importance of shocks and self-gravity in modifying tidal disruption event debris streams. *Monthly Notices of the Royal Astronomical Society*, 526 (2). pp. 2323-2330. ISSN 0035-8711

<https://doi.org/10.1093/mnras/stad2858>

---

© 2023 The Author(s). Reproduced in accordance with the publisher's self-archiving policy.

**Reuse**

Items deposited in White Rose Research Online are protected by copyright, with all rights reserved unless indicated otherwise. They may be downloaded and/or printed for private study, or other acts as permitted by national copyright laws. The publisher or other rights holders may allow further reproduction and re-use of the full text version. This is indicated by the licence information on the White Rose Research Online record for the item.

**Takedown**

If you consider content in White Rose Research Online to be in breach of UK law, please notify us by emailing [eprints@whiterose.ac.uk](mailto:eprints@whiterose.ac.uk) including the URL of the record and the reason for the withdrawal request.



[eprints@whiterose.ac.uk](mailto:eprints@whiterose.ac.uk)  
<https://eprints.whiterose.ac.uk/>

# On the relative importance of shocks and self-gravity in modifying tidal disruption event debris streams

Julia Fancher <sup>1</sup>★, Eric R. Coughlin <sup>1</sup> and C. J. Nixon <sup>2</sup>

<sup>1</sup>*Department of Physics, Syracuse University, Syracuse, NY 13210, USA*

<sup>2</sup>*School of Physics and Astronomy, Sir William Henry Bragg Building, Woodhouse Ln., University of Leeds, Leeds LS2 9JT, UK*

Accepted 2023 September 13. Received 2023 September 12; in original form 2023 July 31

## ABSTRACT

In a tidal disruption event (TDE), a star is destroyed by the gravitational field of a supermassive black hole (SMBH) to produce a stream of debris, some of which accretes onto the SMBH and creates a luminous flare. The distribution of mass along the stream has a direct impact on the accretion rate, and thus modelling the time-dependent evolution of this distribution provides insight into the relevant physical processes that drive the observable properties of TDEs. Analytic models that only account for the ballistic evolution of the debris do not capture salient and time-dependent features of the mass distribution, suggesting that fluid dynamical effects significantly modify the debris dynamics. Previous investigations have claimed that shocks are primarily responsible for these modifications, but here we show – with high-resolution hydrodynamical simulations – that self-gravity is the dominant physical mechanism responsible for the anomalous (i.e. not predicted by ballistic models) debris stream features and its time dependence. These high-resolution simulations also show that there is a specific length-scale on which self-gravity modifies the debris mass distribution, and as such there is enhanced power in specific Fourier modes. Our results have implications for the stability of the debris stream under the influence of self-gravity, particularly at late times and the corresponding observational signatures of TDEs.

**Key words:** black hole physics – hydrodynamics – galaxies: nuclei – transients: tidal disruption events.

## 1 INTRODUCTION

When a star passes within a critical distance of a supermassive black hole (SMBH), it is destroyed by the tidal field – the difference in the gravitational field of the black hole across the diameter of the star – and transformed into a stream of debris (Hills 1975; Rees 1988; see Gezari 2021 for a recent review). This critical distance is typically defined in terms of the tidal radius  $r_t = R_*(M_\bullet/M_*)^{1/3}$ , where  $M_\bullet$  is the mass of the black hole and  $R_*$  and  $M_*$  are the stellar radius and mass, respectively, which arises from equating the stellar surface gravitational field to the tidal acceleration (and dropping order-unity numerical factors). Numerical simulations have shown that, depending on the star’s internal structure and specifically its density profile, the precise distance at which the star is completely destroyed can be slightly larger than or a factor of a few smaller than  $r_t$  (Guillochon & Ramirez-Ruiz 2013; Mainetti et al. 2017; Gollightly, Nixon & Coughlin 2019; Law-Smith et al. 2020; Nixon, Coughlin & Miles 2021). For a TDE in which the star is originally on a parabolic (or near-parabolic) orbit about the SMBH, approximately half of the stellar debris is bound to the SMBH and returns to the point of disruption, where it is expected to circularize into an accretion disc<sup>1</sup>

(e.g. Hayasaki, Stone & Loeb 2013; Shiokawa et al. 2015; Bonnerot et al. 2016; Sądowski et al. 2016; Curd & Narayan 2019; Andalman et al. 2022) and viscously liberate energy at a rate comparable to the Eddington limit of the SMBH (Evans & Kochanek 1989; Wu, Coughlin & Nixon 2018), and we are now detecting many TDEs with surveys such as ZTF (Bellm et al. 2019), ASAS-SN (Shappee et al. 2014), ATLAS (Tonry et al. 2018), eROSITA (Predehl et al. 2021), and (soon) the Rubin Observatory/LSST (Ivezić et al. 2019) (for recent observations of TDEs, see e.g. Komossa & Greiner 1999; Esquej et al. 2007; Gezari et al. 2009, 2012; Bloom et al. 2011; Cenko et al. 2012, 2016; Holoien et al. 2014, 2016; Miller et al. 2015; Alexander et al. 2016; Kara et al. 2016; van Velzen et al. 2016; Blanchard et al. 2017; Gezari, Cenko & Arcavi 2017; Hung et al. 2017, 2020; Pasham et al. 2017, 2019, 2023; Brown et al. 2018; Pasham & van Velzen 2018; Blagorodnova et al. 2019; Nicholl et al. 2019, 2022; Saxton et al. 2019; Wevers et al. 2019, 2021, 2023; Hinkle et al. 2021; van Velzen et al. 2021; Payne et al. 2021; Lin et al. 2022; Hammerstein et al. 2023; Yao et al. 2023).

An analytical model for describing the dynamics of the debris from a TDE, known as the frozen-in approximation and originally due to Lacy, Townes & Hollenbach (1982) (see also Bicknell & Gingold 1983; Stone, Sari & Loeb 2013), treats the interaction between the

\* E-mail: [jlfanche@syr.edu](mailto:jlfanche@syr.edu)

<sup>1</sup>Though the nature of this disc could be very different from a standard, thin disc (Shakura & Sunyaev 1973; Pringle 1981) given the high accretion rates and low binding energy of the returning debris (Loeb & Ulmer 1997; Coughlin & Begelman 2014; Roth et al. 2016; Dai et al. 2018; Steinberg &

Stone 2022; Metzger 2022; Sarin & Metzger 2023), which could help to explain the lower-than-expected temperatures seen from many TDEs; see the discussion regarding TDE optical emission in Gezari (2021) and references therein.

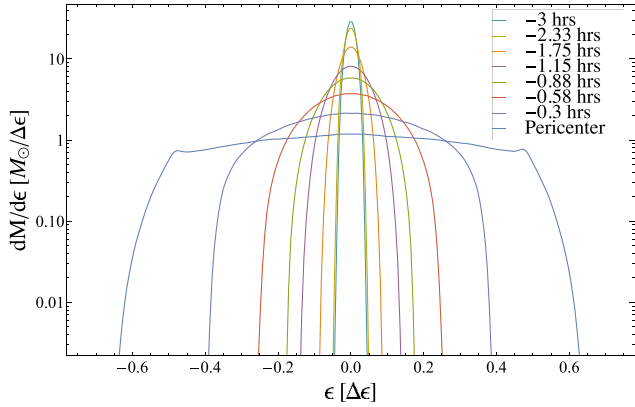


**Figure 1.** The specific energy distribution of the star as it approaches pericentre, calculated from the SPH simulation with 128 million particles. The first time of  $-3$  h (the minus sign indicates that the time is before pericentre) is when the star is at its initial distance of  $5r_t$  from the black hole. We see that the energy spread changes continuously and gradually as the star approaches the black hole, in agreement with Steinberg et al. (2019).

star and the SMBH as occurring instantaneously as the star crosses the tidal sphere of the SMBH. Specifically, at distances much greater than  $r_t$ , the tidal force from the SMBH is assumed to be sufficiently weak that the star retains exact hydrostatic equilibrium, with all of the stellar material moving with the centre of mass. Once the star passes within  $r_t$ , the star is ‘destroyed’, implying that the stellar material moves ballistically in the gravitational field of the SMBH with each gas parcel following an independent Keplerian (or the relativistic generalization) orbit.

The frozen-in approximation predicts that the specific energy of the debris is established at the time the star passes through  $r_t$  (not the pericentre distance, which may be considerably smaller than  $r_t$ , as written in, e.g. Evans & Kochanek 1989; Ulmer 1999; Lodato, King & Pringle 2009; Strubbe & Quataert 2009). Consequently, material with a negative specific energy (or a positive binding energy) – being half of the star in this case – is bound and returns to the SMBH at a rate proportional to  $t^{-5/3}(dM/d\epsilon)$  (Rees 1988; Phinney 1989), where  $t$  is approximately time since disruption and  $dM/d\epsilon$  is the differential amount of mass at a given specific Keplerian binding energy  $\epsilon$ . Since the specific binding energy is conserved in a Keplerian potential, the amount of mass per unit energy,  $dM/d\epsilon$ , is a function only of  $\epsilon$ , and one can use the energy–period relationship for a Keplerian orbit to write  $dM/d\epsilon(t)$ , thereby generalizing the result of Rees (1988) that adopted a constant value for  $dM/d\epsilon$ . Lodato et al. (2009) performed this generalization, and showed that the specific energy distribution could be predicted as a function of the progenitor’s density profile (assumed unaltered until the tidal radius is reached). From their model (see also the black, dashed curves in Figs 2 and 5 below), the stellar debris is expected to have a smooth  $dM/d\epsilon$  curve that is maximized and symmetric about zero, and extends from  $-\Delta\epsilon$  to  $+\Delta\epsilon$ , where  $\Delta\epsilon = GM_\bullet R_\star/r_t^2$  is the maximum specific binding energy to the SMBH. However, Lodato et al. (2009) also ran hydrodynamical simulations of TDEs, and found that their numerically obtained distributions had sharper features than their model predicted, specifically what they termed ‘wings’ that had more mass at larger values of the specific energy than expected. They attributed these discrepancies and additional features in the  $dM/d\epsilon$  curve to shocks in the tidal tails of the stellar debris.

However, the importance of shocks on the dynamics of the debris has recently been questioned by Norman, Nixon & Coughlin (2021),

Coughlin & Nixon (2022), and Kundu, Coughlin & Nixon (2022), who found that even for deep TDEs, in which the stellar pericentre distance is well within the canonical tidal radius, shocks during the compression of the star were either weak with a Mach number near unity or absent completely.<sup>2</sup> Contrarily, it seems possible that the other physical effect ignored in the frozen-in approximation – the self-gravity of the debris stream – could be responsible for the deviation of the numerically obtained  $dM/d\epsilon$  curve from the analytic prediction. Various works have suggested that self-gravity can play an important role in modifying the dynamics of the debris (Kochanek 1994; Guillochon, Manukian & Ramirez-Ruiz 2014; Coughlin et al. 2016; Steinberg et al. 2019) and its hydrodynamic stability (Coughlin & Nixon 2015; Coughlin 2023), and in the extreme case of a partial TDE in which only the outer envelope of the star is tidally stripped, the gravitational influence of the core (i.e. self-gravity) results in a departure of the asymptotic fallback rate from the expected  $\propto t^{-5/3}$  scaling (Guillochon & Ramirez-Ruiz 2013) to  $\propto t^{-9/4}$  (Coughlin & Nixon 2019; Miles, Coughlin & Nixon 2020; Nixon et al. 2021).

Here, we directly assess and isolate the effects of self-gravity versus pressure (i.e. shocks) on the evolution of the debris stream from a TDE and the corresponding fallback rate. In Section 2, we present the results of numerical hydrodynamical simulations of a TDE with and without self-gravity and the resulting evolution of the specific energy distribution or lack thereof, and we conclude in Section 3.

## 2 NUMERICAL SIMULATIONS

### 2.1 Setup

We used the smoothed particle hydrodynamics (SPH) code PHANTOM (Price et al. 2018) to simulate the tidal disruption of a solar-type star (where  $M_\star = M_\odot$  and  $R_\star = R_\odot$ ) by a  $10^6 M_\odot$  SMBH. The star is initially assumed to have a polytropic equation of state with adiabatic index  $\gamma = 5/3$  and is relaxed by allowing the star to evolve in isolation after the polytrope with the desired density profile has been constructed. This lets the internal properties of the star reach equilibrium before it encounters the SMBH. The relaxed star is placed at a distance of  $5r_t$  from the black hole with the centre of mass on a parabolic orbit where the distance from the hole at pericentre is equal to the tidal radius. The gas retains its adiabatic equation of state throughout the TDE. For additional details on the specifics of the SPH kernel and the implementation of self-gravity, see Coughlin & Nixon (2015) and Price et al. (2018).

We ran two sets of simulations with identical initial parameters. In the first set of simulations, self-gravity is included throughout the TDE; in the second, self-gravity is no longer included after the star reaches pericentre. Simulations were performed with a range of particle numbers from 250 thousand to 128 million to assess convergence.

### 2.2 Results

Fig. 1 shows the differential amount of mass per unit energy,  $dM/d\epsilon$ , as a function of the specific Keplerian binding energy,  $\epsilon$ , as the star approaches pericentre (i.e. during its initial ingress through the tidal

<sup>2</sup>It seems likely that a shock forms near the surface following the compression and rebound of the star in deep TDEs, but this only impacts the outer stellar layers (Kobayashi et al. 2004; Guillochon et al. 2009; Yalinewich et al. 2019).

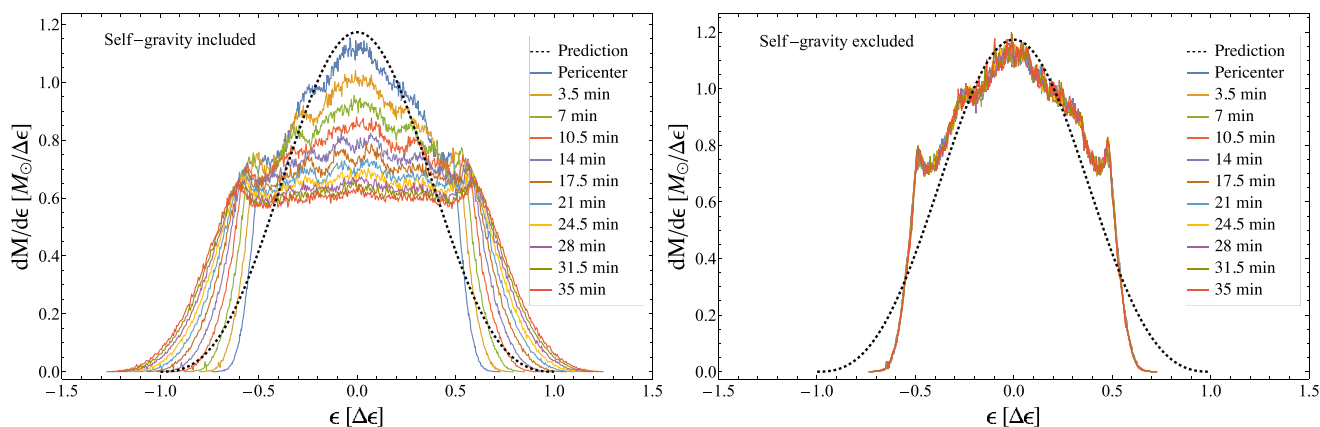


**Figure 2.** The evolution of the specific energy distribution with (left) and without self-gravity (right; self-gravity was turned off at pericentre) at a resolution of 1 million particles. The dashed line shows the predicted  $dM/d\epsilon$  curve calculated from the frozen-in approximation. The approximation is a good fit for the data near pericentre in both cases, but becomes less accurate as the stream evolves with self-gravity.

sphere). The curves are calculated from the SPH simulation with 128 million particles, and we used 500 energy bins evenly spaced between  $-1.5\Delta\epsilon$  and  $1.5\Delta\epsilon$ , where  $\Delta\epsilon = GM_\bullet R_\odot/r_t^2$  is the canonical energy spread from the frozen-in approximation. The legend gives the times at which the energy distributions are calculated, where the minus sign indicates that the star has not yet reached pericentre, and at  $t = -3$  h the star is at a distance of  $5r_t$  from the black hole. For this simulation, self-gravity is included until the star reaches pericentre. In agreement with the results found by Steinberg et al. (2019), we see that the spread in the binding energies of the debris occurs over an extended period of time, reaching a value that is comparable to  $\Delta\epsilon$  when the star is near pericentre. Thus, the approximation that the energy distribution is instantaneously set as the star passes through the tidal radius is rather crude.

The left panel of Fig. 2 shows the  $dM/d\epsilon$  curves calculated every 3.5 min after pericentre from the simulation with 1 million particles and self-gravity included. The predicted  $dM/d\epsilon$  curve indicated by the dashed black line is calculated from the frozen-in approximation as in Lodato et al. (2009). The prediction approximately matches the simulated curve at pericentre (shown in dark blue), but the curves from the simulation immediately evolve to become wider and flatter, making the prediction inaccurate within minutes from disruption. The  $dM/d\epsilon$  curves from the 1 million particle simulation without self-gravity are shown in the right panel of Fig. 2, where the dashed black line is again the prediction. Without self-gravity, the  $dM/d\epsilon$  curve is essentially frozen-in at pericentre, implying that pressure is dynamically insignificant.

Both sets of  $dM/d\epsilon$  curves in Fig. 2 have large fluctuations between  $-\Delta\epsilon/2$  and  $\Delta\epsilon/2$ . To assess whether this feature is related to Poisson noise or physical, we plotted the  $dM/d\epsilon$  curve calculated 35 min after pericentre from simulations with self-gravity included at different resolutions, shown in Fig. 3. It is clear that at lower resolution the amplitude and the number of fluctuations increases, but above 16 million particles the curves are relatively smooth and resemble each other. This implies that while there is some numerical noise related to particle binning, there are underlying physical oscillations in the density of the disrupted stream.

To further assess the convergence of the simulations, in Fig. 4 we over-plotted the  $dM/d\epsilon$  curves from the 16 million (dashed lines) and 128 million (dark solid lines) particle simulations with the  $dM/d\epsilon$  curves from the 1 million particle simulation (light solid lines) as seen in Fig. 2. The colours of the curves match the colours in Fig. 2

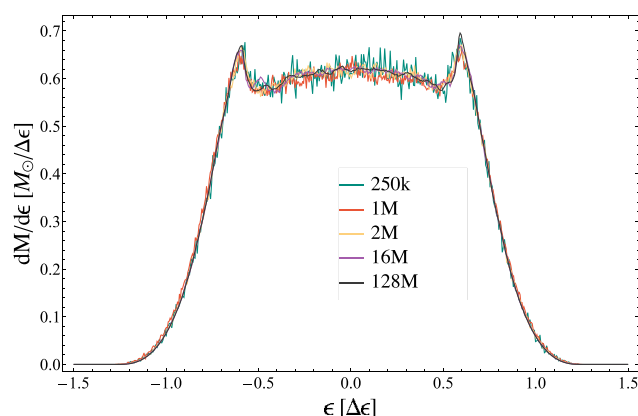


**Figure 3.** The  $dM/d\epsilon$  curve 35 min after pericentre at different resolutions. Note that there are still short-length-scale variations along the debris stream even at high resolutions, which suggests there are physical density oscillations in the disrupted star.

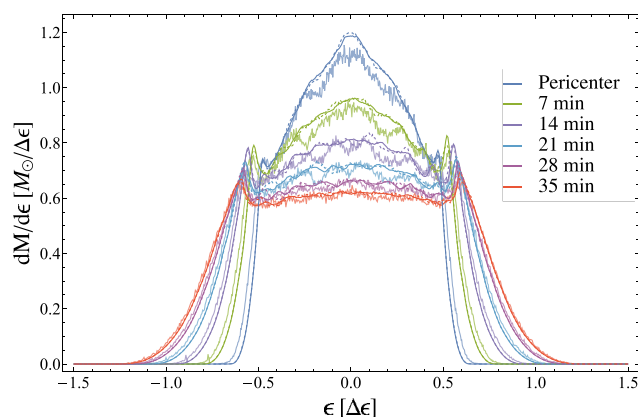


**Figure 4.** The  $dM/d\epsilon$  curves with self-gravity at different resolutions. The lighter solid lines correspond to 1 million particles (Fig. 2), the dashed lines to 16 million particles, and the dark solid lines to 128 million particles.

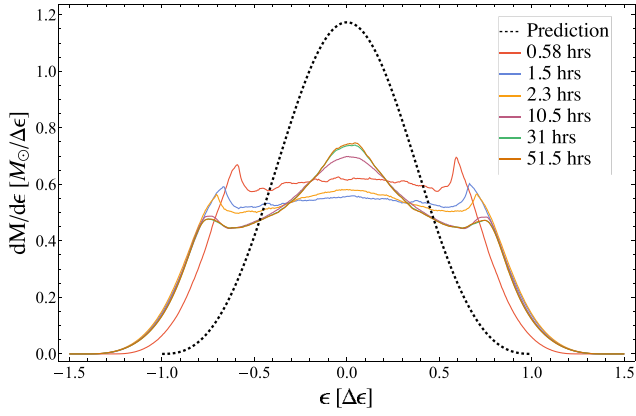


**Figure 5.** The  $dM/d\epsilon$  curves with 128 million particles at later times past pericentre, during which the central peak reforms. After the curve at 51.5 h, the  $dM/d\epsilon$  distribution remains essentially constant for the next 66 d, which marks the end of the simulation.

for the same times. The approximately sinusoidal fluctuations seen between 14 and 21 min in Fig. 2 are still apparent at the 128 million particle resolution, although the feature is now strongest between 21 and 28 min. At all resolutions, this feature is much weaker but still present at 35 min.

Fig. 5 shows the  $dM/d\epsilon$  curves from later times with self-gravity. The  $dM/d\epsilon$  curve continues to flatten until  $\sim 1.5$  h after pericentre, after which time it ‘bounces’ and the central peak begins to reform, suggesting material is coalescing toward the marginally bound radius. By this time, the sinusoidal variations are no longer visibly present, and the curves are much smoother than those around pericentre. Note that the difference in time between successive curves is much greater than that adopted in Fig. 2, and it is only on these much longer time-scales that the  $dM/d\epsilon$  curves show temporal variability. This slowing of the debris stream evolution is consistent with the findings of Coughlin (2023), who found that perturbations on top of the background state of the stream – which is over-stable – vary logarithmically with time. The  $dM/d\epsilon$  curve remains essentially constant from the curve at 51.5 h (seen in Fig. 5) until the end of the simulation, which runs to approximately 68 d. The  $dM/d\epsilon$  curve for later times is wider than the curve at pericentre, and the central peak at later times never reaches the height of the peak at pericentre, meaning the prediction from the frozen-in approximation is inaccurate at later times for both the height of the peak and range of  $\Delta\epsilon$  (note that Lodato et al. 2009 arbitrarily rescaled the height of their frozen-in model to match their numerically obtained  $dM/d\epsilon$  curve at late times, meaning, among other things, that the mass of their frozen-in model did not equal that of their numerical simulation).

The  $dM/d\epsilon$  curves can be used to calculate the fallback rate,  $\dot{M}$ , at a given time after disruption according to (Lodato et al. 2009; Guillochon & Ramirez-Ruiz 2013)

$$\dot{M} = \frac{(2\pi GM_\bullet)^{2/3}}{3} \frac{dM}{d\epsilon} t^{-5/3}, \quad (1)$$

where  $M_\bullet$  is the mass of the black hole and

$$\epsilon(t) = -\frac{1}{2} \left( \frac{2\pi GM_\bullet}{t} \right)^{2/3}. \quad (2)$$

The evolution of the  $dM/d\epsilon$  curve when self-gravity is included therefore results in a changing fallback rate that is not predicted when using the frozen-in approximation (see also the discussion in Guillochon & Ramirez-Ruiz 2013); Wu et al. (2018) showed that

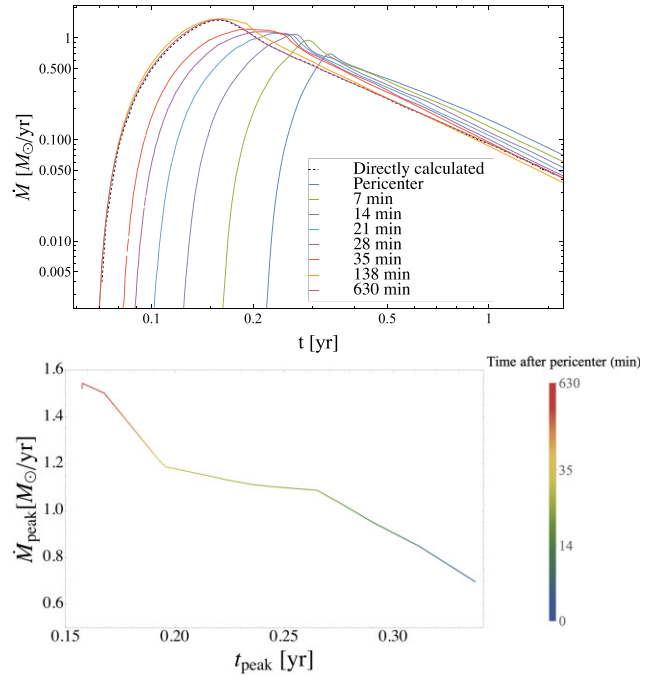


**Figure 6.** Top: The fallback rates calculated from the  $dM/d\epsilon$  curves at the times specified in the legend. The dashed line indicates the fallback rate directly calculated from the 16 million particle run. Bottom: The evolution of the predicted peak fallback rate (calculated from  $dM/d\epsilon$ ) as a function of the time after disruption when the peak is expected to occur. The shading indicates the time at which the fallback rate was calculated, with early times on the right in blue.

the canonical scaling of the fallback rate as  $\propto M_\bullet^{1/2}$ , as discussed in Lacy et al. (1982) and Rees (1988), is accurately recovered for black hole masses between  $10^5 M_\odot \leq M_\bullet \leq 10^7 M_\odot$ ; see specifically their figure 1.<sup>3</sup> The top panel of Fig. 6 plots the evolution of the predicted fallback rates over time calculated with the 128 million particle  $dM/d\epsilon$  curves. As the time at which the  $dM/d\epsilon$  curve is measured shifts to later times, the peak fallback rate increases and occurs earlier while the asymptotic limit of the fallback rate decreases; these two trends are not independent, as a higher peak at earlier times means that less mass will return to the black hole at later times. At very late times this trend reverses slightly, and the fallback rate remains effectively unchanged if the  $dM/d\epsilon$  curve at times greater than  $\gtrsim 630$  min is used. To further illustrate this behaviour, the bottom panel of Fig. 6 shows the peak fallback rate as a function of the time post-disruption at which the peak is predicted to occur. The colour indicates the time after pericentre when the  $dM/d\epsilon$  curve

<sup>3</sup>For either extremely large or extremely small black hole masses, the behaviour shown in Fig. 6 must change qualitatively, as in the large-mass limit relativistic effects will introduce an additional mass dependence, while in the small-mass limit, the fallback time will not be much longer than the dynamical time of the original star. Since self-gravity acts on the latter time-scale (as shown in Fig. 4), if the fallback time is shorter than the dynamical time, self-gravity will not have enough time to modify the energy distribution. Fig. 5 illustrates that the energy distribution does not evolve significantly after  $\sim 10$  h; setting 10 h equal to  $T_{\text{fb}}$ , where  $T_{\text{fb}} = 2\pi (R_\star/2)^{3/2} / \sqrt{GM_\star} \times (M/M_\star)^{1/2}$ , and letting the star be solar-like, yields a mass ratio of  $\sim 100$ . Therefore, we would expect a qualitatively different fallback rate – owing to the inability of self-gravity to act quickly enough – for mass ratios  $\lesssim 100$ .

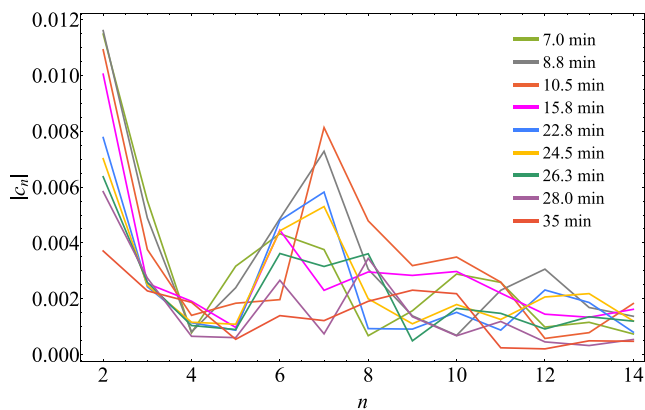


**Figure 7.** The Fourier coefficients calculated from the  $dM/d\epsilon$  curves at the times shown in the legend. The peaks at  $n = 6-8$  displayed by some of the curves indicate enhanced power at wavelengths  $\simeq \Delta\epsilon/n$ .

was used to calculate the fallback rate, with early times in blue and later times in red. The fallback rate predicted under the frozen-in approximation closely aligns with the fallback rate calculated at pericentre, meaning it underestimates the peak fallback rate and overestimates the asymptotic limit shortly after pericentre.

### 2.3 Fourier analysis

It is apparent by eye from Fig. 4 that there is, at early times (between  $\sim 20$  and  $\sim 30$  min post-disruption), a sinusoidal and physical oscillation along the  $dM/d\epsilon$  curve with a wavelength of  $\sim \Delta\epsilon/8$ . To more rigorously assess the strength of this oscillatory feature, we Fourier transform the  $dM/d\epsilon$  curve from the 128 million particle simulation from  $-\Delta\epsilon/2$  to  $\Delta\epsilon/2$ , such that the Fourier coefficients are

$$c_n = \frac{1}{\Delta\epsilon} \int_{-\Delta\epsilon/2}^{\Delta\epsilon/2} \frac{dM}{d\epsilon} e^{-\frac{2\pi i n \epsilon}{\Delta\epsilon}} d\epsilon. \quad (3)$$

Fig. 7 illustrates the Fourier coefficients – normalized by  $c_0$  to offset the declining amount of mass between  $-\Delta\epsilon/2$  and  $\Delta\epsilon/2$  – from  $n = 2-14$  for the times shown in the legend (the colours match those in Figs 2 and 4 for the same times); note that there are points only at integer values of  $n$ , and the lines connecting the points are drawn simply to guide the reader. The coefficients with the largest amplitudes are  $n = 0$ , which yields the (time-dependent) total mass from  $-\Delta\epsilon/2$  to  $\Delta\epsilon/2$ , and  $n = 1$ , which accounts for the quadratic-like peak displayed by the  $dM/d\epsilon$  curves (especially pronounced at the earliest times). We therefore omitted these values of  $n$  from the plot to enhance its readability. This figure demonstrates that, for many of the times indicated in the legend, there is significant and enhanced power at Fourier numbers  $n = 6-8$ , or wavelengths of  $\lambda \simeq \Delta\epsilon/(6-8)$ . However, the power is not static: the largest coefficients occur around times of  $\sim 10$  and  $\sim 25$  min, with a relative minimum near  $\sim 16$  min, and the feature is almost entirely absent by  $\sim 35$  min.

To further highlight the presence of the sinusoidal variation imprinted on the energy distribution, one can high-pass filter the data by subtracting from the  $dM/d\epsilon$  curve the first  $n$  Fourier modes preceding the peak in the power spectrum. The top panel of Fig. 8 illustrates this technique for the  $dM/d\epsilon$  curve at  $t = 22.8$  min post-disruption. In particular, the top-left panel shows the  $dM/d\epsilon$  curve at that time, while the right panel shows the same curve but with the first 6 Fourier modes removed; the dashed curve in the top-right panel illustrates the 7th term in the Fourier series, highlighting

the agreement between this Fourier mode – which has a wavelength of  $\Delta\epsilon/7$  – and the sinusoidal variation of the high-passed data.

In addition to the prominent peak in the power spectrum around a wavelength of  $\Delta\epsilon/7$ , Fig. 7 also shows that there is non-trivial power at higher frequencies, e.g. the solution at a time of 8.8 min post-disruption that has a second prominent peak at  $n = 12$ . The bottom-left panel gives the  $dM/d\epsilon$  curve at this time, while the light-grey curves in the bottom-right panel show the high-passed data up to  $n = 6$  (solid) and the  $n = 7$  Fourier mode (dashed). We scaled the light-grey curves by a factor of 3 to help distinguish them from the dark-grey curves, which show the high-passed data up to  $n = 11$  (solid) and the Fourier mode with  $n = 12$  (dashed). This shows that, while neither mode is immediately apparent in the  $dM/d\epsilon$  curve itself, the sinusoidal variations at these wavelengths are highly significant.<sup>4</sup> This significance is further substantiated by Fig. 9, which shows the power spectrum at  $t = 10.5$  min from the 128M-particle run (solid) and the 16M-particle run; enhanced power at  $n \simeq 7$  is obvious in both cases.

### 3 SUMMARY AND CONCLUSIONS

When a star is destroyed by the gravitational field of a black hole in a TDE, a useful analytical approach for understanding the ensuing dynamics – known as the frozen-in approximation and originally due to Lacy et al. (1982) – assumes that the gas evolves purely ballistically in the gravitational field of the black hole. Under this approximation, the specific Keplerian energy is a conserved Lagrangian (i.e. per-fluid-element) quantity, implying that the binding energy distribution,  $dM/d\epsilon$ , is unaltered from the time of disruption. It was shown by Lodato et al. (2009) that this energy distribution, and the corresponding return rate of gas to the black hole, can be calculated analytically from the density profile of the star. Lodato et al. (2009) also ran smoothed-particle hydrodynamical simulations to test their analytical model and found noticeable discrepancies, among those being the presence of ‘wings’ in the numerically obtained  $dM/d\epsilon$  curve that were absent from the frozen-in prediction. Lodato et al. (2009) attributed these features to one physical effect missing from the frozen-in approximation but included in their hydrodynamical simulations, namely pressure in the form of shocks that putatively occurred near pericentre.

However, there is a second mechanism that can modify the energy distribution of the debris and that was included in the simulations of Lodato et al. (2009), namely the self-gravity of the gas. To investigate which of these two effects – pressure or self-gravity – is predominantly responsible for the presence of the features in the  $dM/d\epsilon$  curve that are not predicted by the frozen-in method, we ran two sets of hydrodynamical simulation of the disruption of a  $\gamma = 5/3$ , polytropic and solar-like star by a  $10^6 M_\odot$  black hole (identical in setup to one of the simulations ran by Lodato et al. 2009). In one set of simulations, self-gravity was turned off after the stellar centre of mass reached pericentre (equal to the canonical tidal radius). In this case, the specific energy distribution of the debris was effectively unchanged (i.e. showed little to no temporal evolution) from the time of pericentre onward and was in overall good agreement with the frozen-in prediction, as shown in the right panel of Fig. 2. Therefore, pressure alone is dynamically insignificant – the specific

<sup>4</sup>Note that the number of bins used to generate the  $dM/d\epsilon$  curves is 500, meaning that the Nyquist frequency corresponds to  $n \simeq 500/6 \simeq 83$ , and hence we are analysing excess power at frequencies well below the values at which we are limited by our bin size.

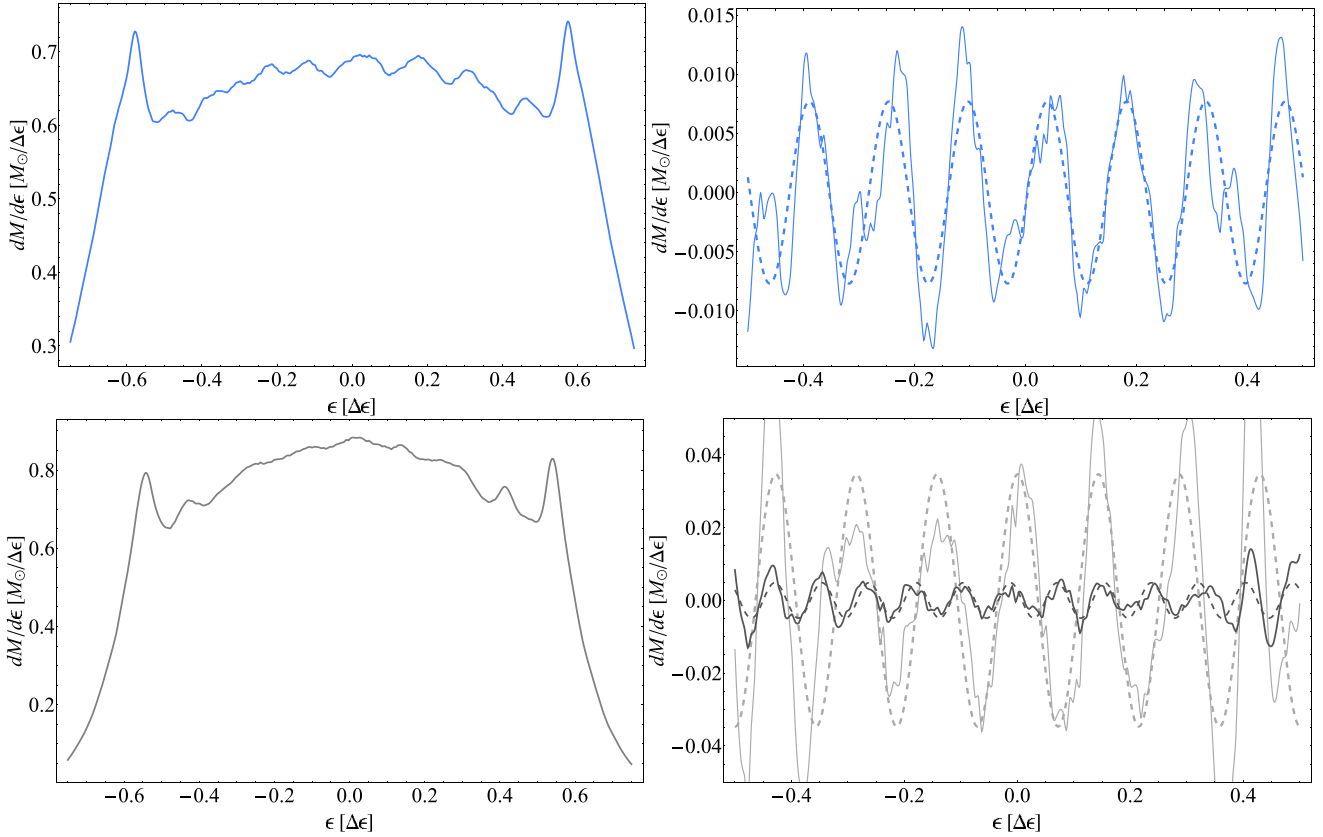


**Figure 8.** Top: The  $dM/d\epsilon$  curve at a time of 22.8 min post-pericentre (left), and the high-passed  $dM/d\epsilon$  curve – where the first 6 Fourier modes are removed (right). The dashed curve in the right panel shows the  $n = 7$  term in the Fourier decomposition, i.e. a sinusoidal curve with a wavelength  $\Delta\epsilon/7$ . Bottom: The  $dM/d\epsilon$  curve at a time of 8.8 min post-pericentre (left), and the high-passed  $dM/d\epsilon$  curve (right); the solid and light-grey curve shows the high-passed solution with the first 6 Fourier modes removed, while the solid and dark-grey curve shows the high-passed data with the first 11 modes removed. The dashed curves show the 7th (light-grey) and 12th (dark-grey) terms in the Fourier expansion. To isolate the curves and increase the clarity of the data, we multiplied the light-grey curves by a factor of 3.

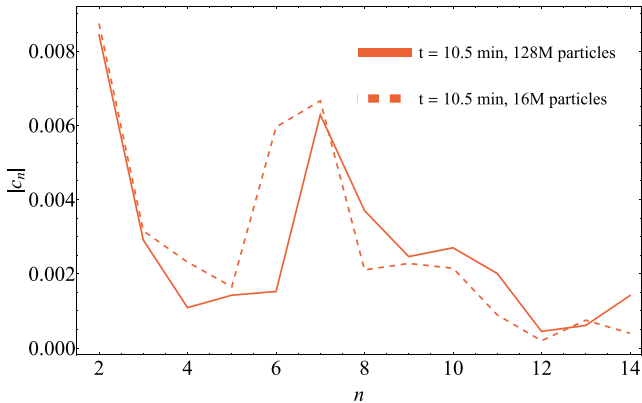


**Figure 9.** The power spectrum at a time of 10.5 min post-disruption, calculated from the  $dM/d\epsilon$  curve with 128 million particles (solid) and 16 million particles (dashed). This highlights the resolution-independence of the excess power at a wavelength in energy of  $\sim\Delta\epsilon/7$ .

Keplerian energy is a conserved Lagrangian variable – and shocks near pericentre are not responsible for producing the deviation in the  $dM/d\epsilon$  curve from the frozen-in prediction.

In a second set of simulations that varied in resolution, from 250 thousand (comparable to the highest resolution employed in Lodato et al. 2009) to 128 million particles, the self-gravity of the gas was

included for the duration of each simulation. In these simulations and as shown in the left-hand panel of Fig. 2, the  $dM/d\epsilon$  curve showed significant temporal evolution, flattening substantially from the initial distribution (which matched that of the pressure-only simulation at pericentre) in the first  $\sim 30$  min (roughly the dynamical time of the original star) after pericentre was reached. At later times a central peak reformed, with the evolution of the debris stream slowing substantially by  $\sim$ few days following pericentre, after which time it agreed with the numerical results of Lodato et al. (2009). We therefore conclude that self-gravity – and in particular the component of the gravitational field that acts along the direction of the stream (see also Steinberg et al. 2019, who similarly argued that the influence of self-gravity along the stream is responsible for the time-dependent modification of the energy spread during the ingress of the star through the tidal sphere) – is the physical mechanism responsible for the evolution of the energy distribution of the debris,<sup>5</sup> and shocks are irrelevant.

<sup>5</sup>There is also an asymmetry in the peaks that form around  $\pm 0.5\Delta\epsilon$ , with the peak at  $+0.5\Delta\epsilon$  systematically higher than that at  $-0.5\Delta\epsilon$ , which is particularly noticeable in the high-resolution simulations in Fig. 3; we thank Matt Todd for pointing this out to us. This asymmetry is likely due to the fact that the shear in the unbound segment of the stream is reduced compared to that in the bound half (Coughlin et al. 2016), rendering self-gravity more capable of modifying the mass distribution.

Self-gravity results in clear sinusoidal variations in the specific energy distribution shortly after the star reaches pericentre; these are apparent by-eye in Fig. 4 around  $\sim 20$  min post-pericentre, and a Fourier analysis of the stream shows increased power on energy scales of  $\sim \Delta\epsilon/7$  (see Figs 7 and 8). On the one hand, increased power at a specific *spatial* scale is not unexpected, as hydrostatic cylinders are gravitationally unstable with a fastest-growing mode that peaks at a wavenumber of  $\sim 1.2H$  for a  $5/3$ -polytropic gas (Coughlin & Nixon 2020), where  $H$  is the cross-sectional radius of the cylinder. If the specific Keplerian energy was exactly conserved, then the energy would correlate with the initial position of a Lagrangian fluid element, and thus we would expect pronounced power on the energy scale that correlates with the length-scale of the most unstable mode. Since the Keplerian energy is not actually a conserved Lagrangian variable (as we have shown in the present analysis) this conclusion is only tentative, but it is suggestive of the fact that this oscillation in energy space is a result of the gravitational instability of the stream. The details (e.g. the growth rate, the dispersion relation) of the instability are significantly more complicated than the hydrostatic case owing to the presence of the shear along the filament axis, but the recent work of Coughlin (2023) has shown that the stream is overstable in the cylindrical-radial direction, and it is plausible that the oscillation in energy space identified here is a manifestation of an analogous instability along the filament axis.

## ACKNOWLEDGEMENTS

We thank Matt Todd for a useful comment regarding the asymmetry of the mass distribution in the stream, and we thank the referee, Elad Steinberg, for useful comments that added to the quality of our work. JF acknowledges support from Syracuse University through the SOURCE programme and a Young Research Fellows award. ERC acknowledges support from the National Science Foundation through grant AST-2006684, and the Oakridge Associated Universities for their support through a Ralph E. Powe Junior Faculty Enhancement Award. CJN acknowledges support from the Science and Technology Facilities Council (grant number ST/Y000544/1), and the Leverhulme Trust (grant number RPG-2021-380). Part of this research made use of the DiRAC Data Intensive service at Leicester, operated by the University of Leicester IT Services, which forms part of the Science and Technology Facilities Council (STFC) DiRAC HPC Facility ([www.dirac.ac.uk](http://www.dirac.ac.uk)). The equipment was funded by BEIS capital funding via STFC capital grants ST/K000373/1 and ST/R002363/1 and STFC DiRAC Operations grant ST/R001014/1. DiRAC is part of the National e-Infrastructure.

## DATA AVAILABILITY

The simulations in this paper can be reproduced by using the PHANTOM code (Astrophysics Source Code Library identifier ascl.net/1709.002). The data underlying this article will be shared on reasonable request to the corresponding author.

## REFERENCES

- Alexander K. D., Berger E., Guillochon J., Zauderer B. A., Williams P. K. G., 2016, *ApJ*, 819, L25
- Andalman Z. L., Liska M. T. P., Tchekhovskoy A., Coughlin E. R., Stone N., 2022, *MNRAS*, 510, 1627
- Bellm E. C. et al., 2019, *PASP*, 131, 018002
- Bicknell G. V., Gingold R. A., 1983, *ApJ*, 273, 749
- Blagorodnova N. et al., 2019, *ApJ*, 873, 92
- Blanchard P. K. et al., 2017, *ApJ*, 843, 106
- Bloom J. S. et al., 2011, *Science*, 333, 203
- Bonnerot C., Rossi E. M., Lodato G., Price D. J., 2016, *MNRAS*, 455, 2253
- Brown J. S. et al., 2018, *MNRAS*, 473, 1130
- Cenko S. B. et al., 2012, *ApJ*, 753, 77
- Cenko S. B. et al., 2016, *ApJ*, 818, L32
- Coughlin E. R., 2023, *MNRAS*, 522, 5500
- Coughlin E. R., Begelman M. C., 2014, *ApJ*, 781, 82
- Coughlin E. R., Nixon C., 2015, *ApJ*, 808, L11
- Coughlin E. R., Nixon C. J., 2019, *ApJ*, 883, L17
- Coughlin E. R., Nixon C. J., 2020, *ApJS*, 247, 51
- Coughlin E. R., Nixon C. J., 2022, *ApJ*, 926, 47
- Coughlin E. R., Nixon C., Begelman M. C., Armitage P. J., Price D. J., 2016, *MNRAS*, 455, 3612
- Curd B., Narayan R., 2019, *MNRAS*, 483, 565
- Dai L., McKinney J. C., Roth N., Ramirez-Ruiz E., Miller M. C., 2018, *ApJ*, 859, L20
- Esquej P., Saxton R. D., Freyberg M. J., Read A. M., Altieri B., Sanchez-Portal M., Hasinger G., 2007, *A&A*, 462, L49
- Evans C. R., Kochanek C. S., 1989, *ApJ*, 346, L13
- Gezari S. et al., 2009, *ApJ*, 698, 1367
- Gezari S. et al., 2012, *Nature*, 485, 217
- Gezari S., 2021, *ARA&A*, 59, 21
- Gezari S., Cenko S. B., Arcavi I., 2017, *ApJ*, 851, L47
- Golightly E. C. A., Nixon C. J., Coughlin E. R., 2019, *ApJ*, 882, L26
- Guillochon J., Ramirez-Ruiz E., 2013, *ApJ*, 767, 25
- Guillochon J., Ramirez-Ruiz E., Rosswog S., Kasen D., 2009, *ApJ*, 705, 844
- Guillochon J., Manukian H., Ramirez-Ruiz E., 2014, *ApJ*, 783, 23
- Hammerstein E. et al., 2023, *ApJ*, 942, 9
- Hayasaki K., Stone N., Loeb A., 2013, *MNRAS*, 434, 909
- Hills J. G., 1975, *Nature*, 254, 295
- Hinkle J. T. et al., 2021, *MNRAS*, 500, 1673
- Holoien T. W. S. et al., 2014, *MNRAS*, 445, 3263
- Holoien T. W. S. et al., 2016, *MNRAS*, 463, 3813
- Hung T. et al., 2017, *ApJ*, 842, 29
- Hung T. et al., 2020, *ApJ*, 917, 9
- Ivezić Ž. et al., 2019, *ApJ*, 873, 111
- Kara E., Miller J. M., Reynolds C., Dai L., 2016, *Nature*, 535, 388
- Kobayashi S., Laguna P., Phinney E. S., Mészáros P., 2004, *ApJ*, 615, 855
- Kochanek C. S., 1994, *ApJ*, 422, 508
- Komossa S., Greiner J., 1999, *A&A*, 349, L45
- Kundu S. K., Coughlin E. R., Nixon C. J., 2022, *ApJ*, 939, 71
- Lacy J. H., Townes C. H., Hollenbach D. J., 1982, *ApJ*, 262, 120
- Law-Smith J. A. P., Coulter D. A., Guillochon J., Mockler B., Ramirez-Ruiz E., 2020, *ApJ*, 905, 141
- Lin Z., Jiang N., Kong X., Huang S., Lin Z., Zhu J., Wang Y., 2022, *ApJ*, 939, L33
- Lodato G., King A. R., Pringle J. E., 2009, *MNRAS*, 392, 332
- Loeb A., Ulmer A., 1997, *ApJ*, 489, 573
- Mainetti D., Lupi A., Campana S., Colpi M., Coughlin E. R., Guillochon J., Ramirez-Ruiz E., 2017, *A&A*, 600, A124
- Metzger B. D., 2022, *ApJ*, 937, L12
- Miles P. R., Coughlin E. R., Nixon C. J., 2020, *ApJ*, 899, 36
- Miller J. M. et al., 2015, *Nature*, 526, 542
- Nicholl M. et al., 2019, *MNRAS*, 488, 1878
- Nicholl M., Lanning D., Ramsden P., Mockler B., Lawrence A., Short P., Ridley E. J., 2022, *MNRAS*, 515, 5604
- Nixon C. J., Coughlin E. R., Miles P. R., 2021, *ApJ*, 922, 168
- Norman S. M. J., Nixon C. J., Coughlin E. R., 2021, *ApJ*, 923, 184
- Pasham D. R. et al., 2019, *Science*, 363, 531
- Pasham D. R. et al., 2023, *Nat. Astron.*, 7, 88
- Pasham D. R., van Velzen S., 2018, *ApJ*, 856, 1
- Pasham D. R., Cenko S. B., Sadowski A., Guillochon J., Stone N. C., van Velzen S., Cannizzo J. K., 2017, *ApJ*, 837, L30
- Payne A. V. et al., 2021, *ApJ*, 910, 125
- Phinney E. S., 1989, in Morris M., ed., Proc. IAU Symp. 136, The Center of the Galaxy. Kluwer, Dordrecht, 543

- Predehl P. et al., 2021, *A&A*, 647, A1  
Price D. J. et al., 2018, *Publ. Astron. Soc. Aust.*, 35, e031  
Pringle J. E., 1981, *ARA&A*, 19, 137  
Rees M. J., 1988, *Nature*, 333, 523  
Roth N., Kasen D., Guillochon J., Ramirez-Ruiz E., 2016, *ApJ*, 827, 3  
Sarin N., Metzger B. D., 2023, preprint ([arXiv:2307.15121](https://arxiv.org/abs/2307.15121))  
Saxton R. D. et al., 2019, *A&A*, 630, A98  
Shakura N. I., Sunyaev R. A., 1973, *A&A*, 24, 337  
Shappee B. J. et al., 2014, *ApJ*, 788, 48  
Shiokawa H., Krolik J. H., Cheng R. M., Piran T., Noble S. C., 2015, *ApJ*, 804, 85  
Steinberg E., Stone N. C., 2022, preprint ([arXiv:2206.10641](https://arxiv.org/abs/2206.10641))  
Steinberg E., Coughlin E. R., Stone N. C., Metzger B. D., 2019, *MNRAS*, 485, L146  
Stone N., Sari R., Loeb A., 2013, *MNRAS*, 435, 1809  
Strubbe L. E., Quataert E., 2009, *MNRAS*, 400, 2070  
Sądowski A., Tejada E., Gafton E., Rosswog S., Abarca D., 2016, *MNRAS*, 458, 4250  
Tonry J. L. et al., 2018, *PASP*, 130, 064505  
Ulmer A., 1999, *ApJ*, 514, 180  
van Velzen S. et al., 2016, *Science*, 351, 62  
van Velzen S. et al., 2021, *ApJ*, 908, 4  
Wevers T. et al., 2019, *MNRAS*, 488, 4816  
Wevers T. et al., 2021, *ApJ*, 912, 151  
Wevers T. et al., 2023, *ApJ*, 942, L33  
Wu S., Coughlin E. R., Nixon C., 2018, *MNRAS*, 478, 3016  
Yalinewich A., Guillochon J., Sari R., Loeb A., 2019, *MNRAS*, 482, 2872  
Yao Y. et al., 2023, preprint ([arXiv:2303.06523](https://arxiv.org/abs/2303.06523))

This paper has been typeset from a  $\text{\TeX}/\text{\LaTeX}$  file prepared by the author.